

Inertial Piezoelectric Actuation of a Needle Insertion Device for Minimally Invasive Surgery*

Yuzhou Duan, Hongtao Peng, Yuchuan Zhu, Yayi Shen, and Jie Ling

Abstract—Robotic-assisted needle intervention has shown great prospects in minimally invasive surgery (MRI), where the needle insertion device (NID) is an important component. Some sophisticated intervention practices require the NID to have the characteristics of high resolution, enough insertion force, and compact structure. In this work, a NID driven by an inertial piezoelectric actuator is developed and validated by experiments. The actuator consists of a triangular configured compliant driving mechanism and a piezoelectric stack installed inside to meet the requirements. A prototype with a compact structure of $86 \times 104 \times 41 \text{ mm}^3$ is fabricated to test the performance of the proposed NID. Both the no-load test and phantom test are carried out. Experimental results show that the developed NID reaches a resolution of 4.7 nm (fine positioning mode), a maximum velocity of 6.89 mm/s, and a maximum insertion force of 2.4 N. The resolution and structure volume are superior to the traditional NID, and the insertion force is higher than the same type of NID. A potential application of the proposed NID is high-precision needle intervention with limited working space, such as MRI-based needle biopsy.

I. INTRODUCTION

For minimally invasive surgery, needle intervention is a widely used medical practice in which a needle is inserted into the body for subsequent diagnosis and therapy. Assisted by robots, this practice has revealed its unique advantages in some promoting fields such as eye, ear, and lumbar surgery [1]–[3]. The upsides of working in tandem with robots lie in many aspects: 1) avoiding problems of physiological hand tremor [4], 2) performing higher precision insertion angle and depth in comparison with surgeons [5], and 3) presenting sophisticated insertion motions to raise surgical performance [6]. A needle insertion device (NID) is one of the important components in robotic-assisted needle intervention. This NID can be designed separately for handheld [7] or can be integrated into surgical robots as the end effector [8]. The latter form is more common and more recognized to realize the higher autonomy of surgical robots.

The basic motion of the NID is the translational insertion motion, which is commonly implemented by a motor-driven ball screw linear guide [7], [9], [10]. However, the large mass of the motor and transmission mechanism limits the miniaturization of the surgical robot, increases the end inertia, and blocks the view of surgeons [11]. Except for the translational motion, NIDs can be designed with a richer set of functions for specific needs, including master-slave design

for teleoperation in magnetic resonance imaging (MRI) environment [12], axial rotation design for bone surgery and needle steering requirements [13], and vibration design to reduce insertion force as well as increase accuracy [14].

Piezoelectric motors have been used in the needle insertion field due to the advantages of high accuracy, high frequency response, compact size, and MRI compatibility. In [15], a 2-DOF (degree of freedom) piezoelectric motor is proposed for MRI-guided insertion. This inchworm-type motor uses four piezo stacks and achieves a linear speed of 5.4 mm/s and a rotary speed of 10.5 rpm. In [16], phase change material (wax) has been used together with piezo stacks to realize inchworm motion. The actuator is rather small in vitro of the novel principle, making it capable of eye-mounted applications. However, the limitation of existing inchworm-type piezoelectric motor lies in the inborn structure with multiple piezo stacks so that the time sequence of the excitation signals is complex [17].

Except for the inchworm type, inertial piezoelectric actuators are also introduced for needle insertion. In [18], the rotation motion of a tip-separated needle is realized by this kind of actuator. Recently, a 2-DOF NID using inertial piezoelectric actuators has been proposed [19]. The needle is driven based on stick-slip motion, which owns the advantages of a relatively simple structure and control over an inchworm type. Correspondingly, however, the driving force is reduced (32 mN). The small blocking force limits the usage of the inertial piezoelectric actuators in most needle intervention scenarios.

To take advantage of the compact structure and high resolution of an inertial piezoelectric actuator, and to simultaneously address the problem of a small blocking force of existing inertial piezoelectric actuators, this paper develops and validates a NID based on the inertial piezoelectric actuator. A triangular compliant driving mechanism proposed in [20] is integrated to output the required driving force during insertion. Experiments are conducted to evaluate the kinematic and mechanical performances in both the no-load and phantom tests. The developed NID is hopeful to broaden the application of inertial piezoelectric actuation in needle intervention. The contribution of this paper can be concluded in threefold:

- Developing a compact NID based on the inertial piezoelectric actuator with large insertion force;
- Validating the performance of the NID experimentally by no-load test and tissue phantom test;
- Presenting the relationship between the insertion force and driving voltage, driving frequency, and pre-load of

*This work was supported by the Natural Science Foundation of Jiangsu Province (Grant No. BK20210294).

The authors are with the College of Mechanical & Electrical Engineering, Nanjing University of Aeronautics and Astronautics, Nanjing 210016, China. (Corresponding author: Jie Ling. e-mail: meeijing@nuaa.edu.cn)

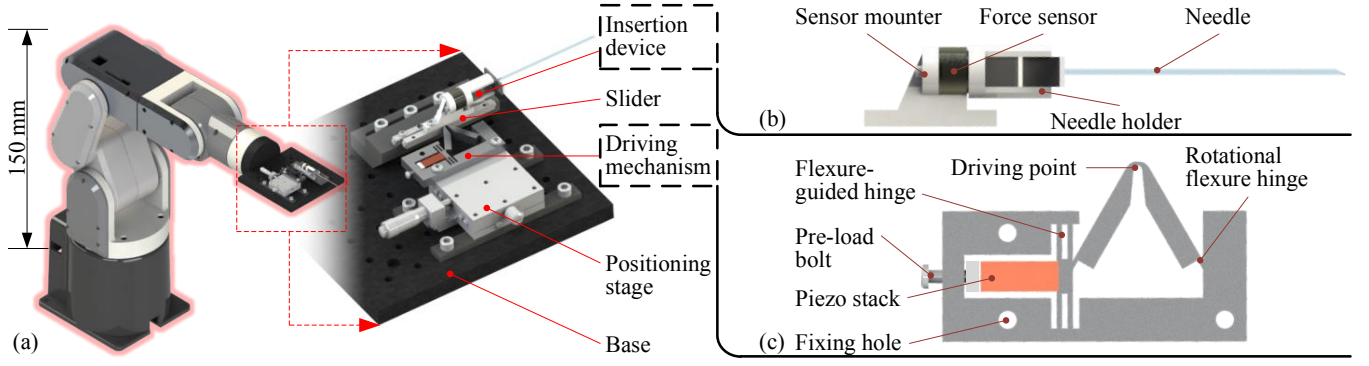


Fig. 1. Schematic diagram of the proposed insertion device. (a) Device configuration. (b) Insertion structure. (c) Triangular compliant driving mechanism.

the proposed NID.

The remainder is organized as follows. Section II introduces the configuration of the NID and illustrates the working principle of the triangular compliant driving mechanism. In Section III, detailed experiments are conducted to validate the performance of the proposed NID, including no-load tests and phantom tests. At last, the discussion and conclusion remark is made in Section IV.

II. DEVICE CONFIGURATION AND WORKING PRINCIPLE

In this section, the configuration and working principle of the proposed NID is described.

A. Device Configuration

Figure 1(a) presents the schematic diagram of the proposed NID. Due to its compact structure, this NID is intended as an end effector for a desktop level robotic manipulator. The manipulator is used for insertion point positioning and the NID is used to insert the needle. The main parts of the NID include the insertion structure, slider, driving mechanism, positioning stage, and base. The x-axis positioning stage is mounted on the base, providing support and a controllable pre-load to the driving mechanism. Actuated by the driving mechanism, the slider moves forward with the needle insertion mechanism fixed on it. The NID and driving mechanism are then introduced in detail as follows.

As shown in Fig. 1(b), the NID is magnified. The needle is mounted on the needle holder, which is connected to a force sensor to measure the insertion force. All the above parts are fixed on the sensor holder. As shown in Fig. 1(c), a pre-load bolt is applied to install the piezo stack (a spacer is sandwiched to prevent stress concentration). The rest part is a compliant mechanism (CM), which transmits the motion of the piezo stack to the driving point. The transmission is realized by the flexure hinges. The flexure-guide hinge provides pre-load and the two rotational flexure hinges are the main deformation regions to transmit motion.

B. Working Principle

The working principle of the driving mechanism is illustrated in Fig. 2. Of note, the principle has been introduced in detail in [20] and [21]. Here, we only made a brief illustration. The piezo stack is actuated by a periodic sawtooth

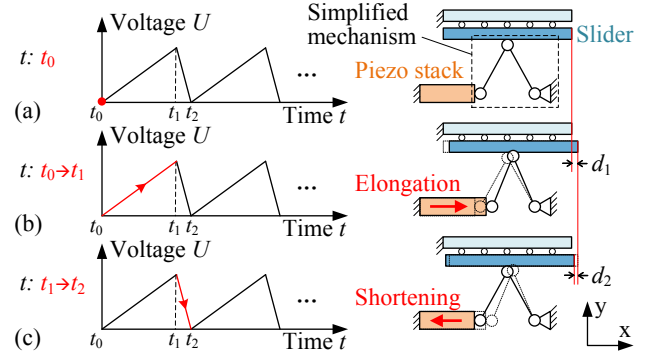


Fig. 2. Working principle of the triangular compliant driving mechanism.

waveform voltage signal, of which three distinct stages can be divided: the initial stage, slow forward stage, and fast backward stage.

As shown in Fig. 2(a), it is the initial stage of the driving cycle. The driving point is in contact with the slider. The flexure-guided hinges are neglected because they only provide the guide effect. The rest parts of the CM are simplified into a rigid body mechanism characterized by triangular linkages according to the pseudo-rigid body method. No voltage is applied to the piezo stack.

As shown in Fig. 2(b), it presents the slow forward stage of the driving cycle (from t_0 to t_1). The piezo stack extends slowly in the x-axis as the input of the CM. The output of the CM (e.i., the driving point) possesses the components of motion in both the y and x directions. The former component clamps the slider (the motion in y direction is absorbed by the CM) and the latter moves the slider forward due to the static friction between the driving point and the slider. In Fig. 2(b), the total displacement of the slider is marked as d_1 .

As shown in Fig. 2(c), it presents the fast backward stage of the driving cycle (from t_1 to t_2). The voltage U applied to the piezo stack rapidly reduces from peak to zero, resulting in a fast shorting of the piezo stack. Initially, the slider keeps moving forward due to inertia, while the driving point moves backward because of the shortening of the piezo stack. Thus, there is dynamic friction between the drive point and the slider, inhibiting the movement of the slider and producing

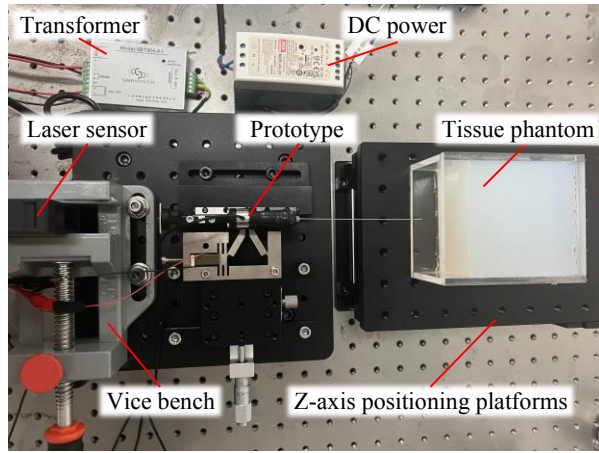


Fig. 3. Experimental system of the proposed needle insertion device.

a certain backward motion. In Fig. 2(c), the backward loss of displacement is marked as d_2 .

Through the above analysis, a period of forward displacement can be obtained in one cycle, represented by $d_c = d_2 - d_1$ (Small figure of Fig. 5 for embodiment). Theoretically, the slide can realize infinite displacement by repeating the three steps of motion.

III. EXPERIMENTS

In this section, experiments are carried out to validate the proposed NID and explore the relationship between insertion force and key parameters including driving voltage, driving frequency, and pre-load.

A. Prototype and Experimental Setup

Figure 3 presents the experiment system of the needle insertion into tissue phantom by the designed prototype. The CM of the prototype is made of 45 steel and fabricated via wire-cut electrical discharge machining. The piezo stack (SA070718, PiezoDrive Co., Ltd., Australia) works in longitudinal mode. The cross-roller slider (VR2-75HX13Z, THK Co., Ltd., Japan) is chosen to guide the needle insertion due to its high stiffness and linearity. The CM is mounted on an x-axis positioning stage (SAMLO Co., Ltd., China) to modify the pre-load.

The needle force sensor is mounted on the slider by two customized mounters, which are resin and fabricated by 3D print technology (type 8000, Wenext Co., Ltd., China). The 1-DOF force sensor (SBT674 SIMBATOUCH Co., Ltd., China) is fixed at the bottom of the needle to collect the axial force during insertion. A medical-graded lumbar puncture needle with an outer diameter of 0.7 mm is used to validate the insertion performance. The tissue phantom is made of medical silicone (PS6600, YIPINGYIPING Co., Ltd., China). A Z-axis positioning platform is used to control the height of the tissue phantom to achieve different insertion entries. The displacement is measured by a laser sensor (CD33-120NV, OPTEX Co., Ltd., Japan) mounted on a vice bench with an accuracy of 120 μm . A capacitive displacement sensor (E09.CAP200, Core Tomorrow Co., Ltd., China)

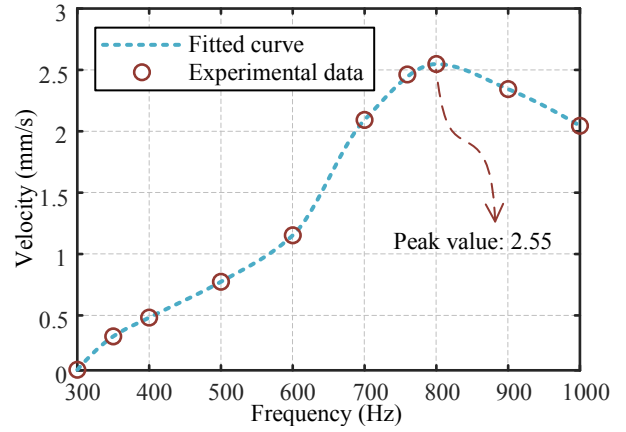


Fig. 4. No-load test of the relationship between the driving frequency and the slider velocity with the applied voltage of 60 V.

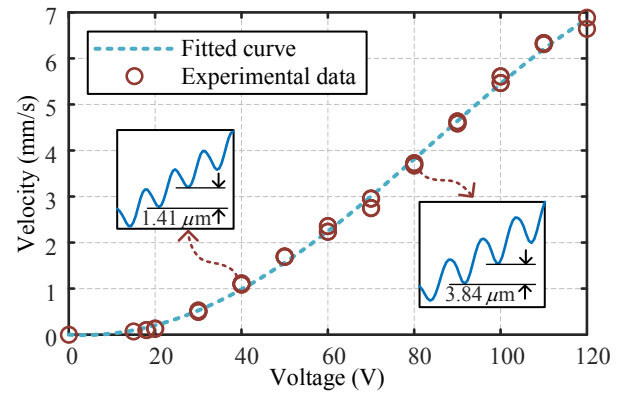


Fig. 5. No-load test of the relationship between the applied voltage and the slider velocity with the driving frequency of 800 Hz.

with a static resolution of 2.5 nm is used to measure the displacement microscopically, which takes the place of the laser sensor when used.

A function generator (DG1022U, RIGOL Co., Ltd., China) is used to generate the required signal, which is amplified by a power amplifier (7224, AE Techtron Inc., USA) as the input voltage signal of the piezo stack. Signals of the force sensor and displacement sensor are collected by a data acquisition card (PCI-6259, NI Inc., USA). The asymmetry of the sawtooth wave is set to 90%.

B. No-Load Test

The no-load tests were first conducted to evaluate the performance of the driving mechanism. The relationship between the insertion velocity and driving frequency with a constant voltage of 60 V is presented in Fig. 4. The applied frequency is from 300 Hz to 1000 Hz, which is the suitable frequency band for insertion. At lower frequencies, the guide slider no longer moves, and at higher frequencies, it is difficult for the needle to penetrate the tissue. Each experimental data is tested three times to obtain the average value. The maximum insertion speed occurs with the driving frequency of 800 Hz in the figure.

The relationship between the insertion velocity and applied

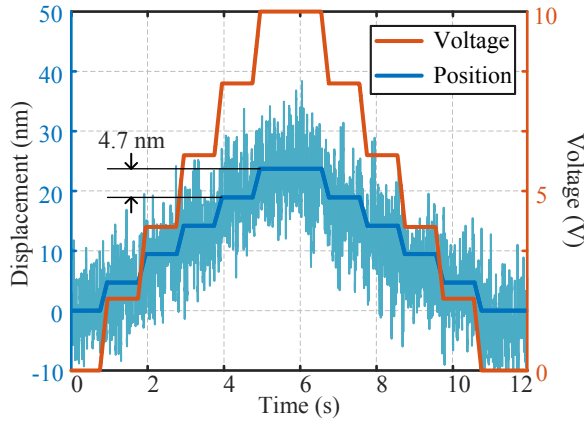


Fig. 6. Measuring resolutions with stairs-shaped waves.

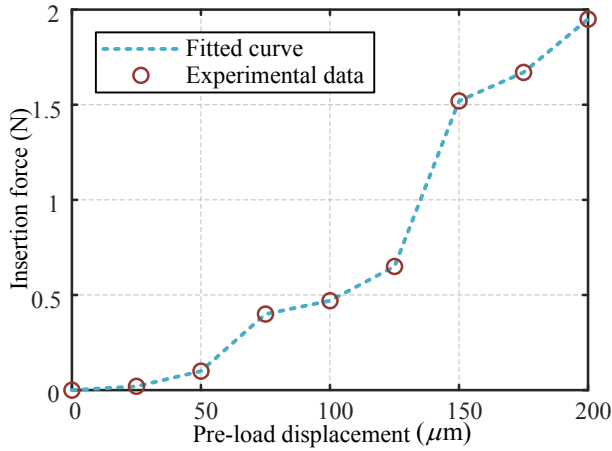


Fig. 7. Phantom test of the relationship between the pre-load and the insertion force with the driving frequency of 1000 Hz and voltage of 80 V.

voltage of the input signal with a constant frequency of 800 Hz (optimal frequency according to the above analysis) is presented in Fig. 5. The experiment is repeated twice at each voltage point and both are presented in the figure. The results show that there is a good linear relationship between velocity and voltage when the voltage is greater than 40 V. However, at the initial stage (i.e., from 0 to 30 V) the speed increases slowly with the voltage. This “dead zone” is because the pre-load force cannot be precisely adjusted (Increasing the pre-load can improve this situation). Additionally, The asymmetry of the assembly and the friction between the slider leads to a certain starting voltage. The subsequent linear part of the fitting curve is easy to explain. As shown in the small image of Fig. 5, the single stick-slip motion increases linearly with the increase of voltage. Macroscopically, a linearly increased velocity can be acquired. Within the allowed voltage of the piezo stack, the maximum no-load speed of 6.89 mm/s is measured.

The insertion motion is realized by applying a sawtooth waveform voltage signal to the piezo stack (marked as insertion mode). After reaching the target, a fine positioning mode could be realized to modify the tip position precisely. This mode is conducted by applying a continuous voltage signal

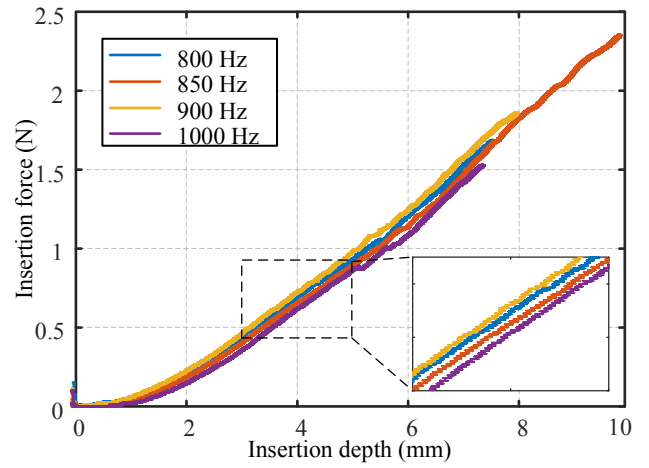


Fig. 8. Phantom test of the relationship between the insertion depth and the insertion force with the driving voltage of 100 V under different driving frequencies.

to the piezo stack. In vitro of the static friction between the driving point and slider to achieve more accurate positioning than the insertion mode. To validate the feasibility of this mode, we perform a stairs-shaped-wave test to measure the resolutions of the NID. The voltage of each stair is 2 V (the smallest stair the sensor can measure) and the output position is processed by filtering and fitting steps. The result is shown in Fig. 6, of which the fitted resolution is 4.7 nm.

C. Phantom Test

Except for the no-load test, the insertion performance through load tests is validated in the tissue phantom. The pre-load (characterized by the feeding displacement of the x-axis positioning stage) between the driving CM and the slider directly influences the insertion force by increasing the friction at the driving point. Fig. 7 depicts this feature under the driving frequency of 1000 Hz and the driving voltage of 80 V. The insertion force increases nonlinearly with the increase of the pre-load displacement. In the absence of any pre-load, the insertion depth is almost zero. This nonlinear relationship is caused by the fact that the optimal driving voltage varies with the change of the pre-load. This issue is talked about later in Fig. 9. The relationship between insertion depth and insertion force is tested under the pre-load distance of 150 μm under different driving frequencies. The result is shown in Fig. 8, in which these insertion curves are similar. This relationship is also tested under different driving voltages, leading to the same results. These tests indicate that the force-depth relationship is independent of the driving parameters of the piezoelectric actuator. Notably, it is found that these curves can be well-fitted by third-order polynomials, which conflicts with the fitting with a quadratic polynomial mentioned in [22].

The relationship between the driving voltage and the insertion force is studied. Fig. 9 presents this relationship under the driving frequency of 1000 Hz and the pre-load displacement of 100, 150, and 200 μm . The results show

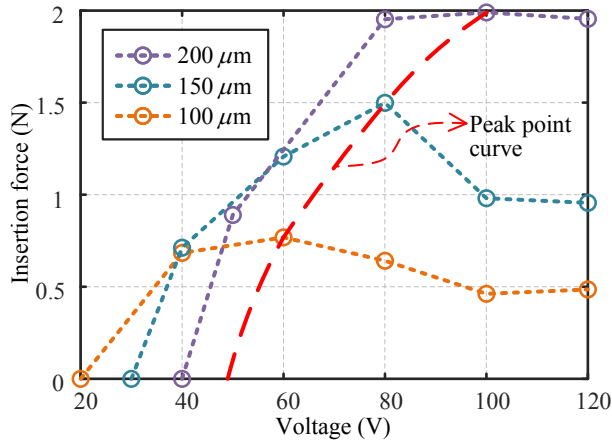


Fig. 9. Phantom test of the relationship between the applied voltage and the insertion force with the driving frequency of 1000 Hz.

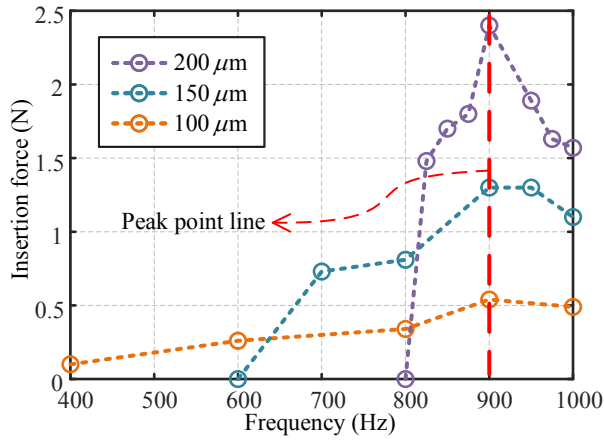


Fig. 10. Phantom test of the relationship between the driving frequency and the insertion force with the driving voltage of 80 V.

that the insertion force initially increases with the increase of voltage, and then decreases slightly after an optimal voltage. The maximum insertion force also increases as the pre-load displacement increases. Of note, the optimal voltage increases with the increase of pre-load (the peak point curve in the figure). Additionally, the “dead zone” of the voltage increases when the pre-load goes larger. The above analysis indicates that the optimal driving voltage and the pre-load have a positive correspondence to reach the maximum insertion force.

The relationship between the driving frequency and the insertion force is also investigated. As shown in Fig. 10, which presents this relationship under the driving voltage of 100 V and the pre-load displacement of 50, 100, and 150 μm . The results show similarity with the trend of the relationship between the applied voltage and the insertion force analyzed above, i.e., the insertion force initially increases with the increase of the frequency and then decreases after an optimal value. Additionally, these curves also have “dead zones”, which increase with the pre-load. However, the difference lies in the phenomenon that the pick point curve in Fig.

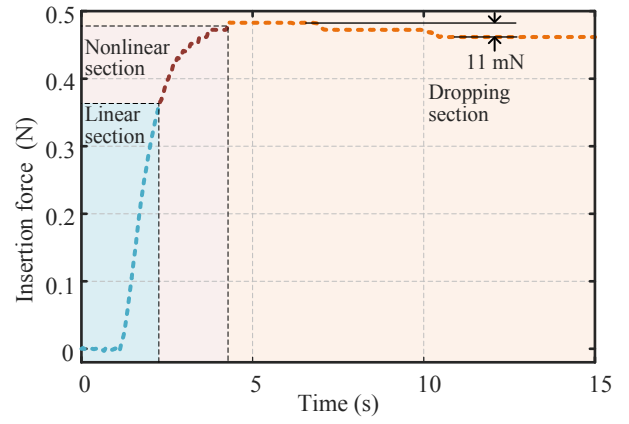


Fig. 11. Phantom test of the insertion force related to time with the driving voltage of 100V, frequency of 1000 Hz, and pre-load displacement of 100 μm .

10 is a straight line, which means the optimal frequency is independent of pre-load displacement. In the testing range of this paper, the maximum insertion force occurs in this figure, which is 2.4 N.

IV. DISCUSSION AND CONCLUSION

In this section, the results of the experimental tests as well as key issues in needle interventions are first discussed. Then, the work of this paper is concluded, and future work on this inertial piezoelectric actuated NID is discussed.

A. Discussion

Although the feasibility of the proposed NID is validated through no-load and phantom tests, some important issues need to be discussed hereunder.

First, the maximum insertion force of different needle interventions varies greatly (e.g., sclera force of around 400 mN in eye surgery [23] and around 50 N in bone surgery [24]). In this paper, the maximum force is 2.4 N, which is still too small to be implemented in some applications. To further increase the insertion force, approaches include increasing structure stiffness, increasing inertial mass, and further increasing the pre-load can be considered. Of note, the actual allowable insertion force should be a little less than the maximum insertion force. The reasons are twofold and are presented in Fig. 11. On the one hand, the insertion depth-time curve becomes nonlinear when approaching the maximum insertion force (the nonlinear section). On the other hand, there is a small “rebound” phenomenon (the drop section) after reaching the maximum insertion force (or depth). Influenced by the maximum insertion force, the insertion depth of this NID is limited (10 mm). For some deep tissue insertion requirements such as lumbar puncture of around 60 mm [25], this insertion depth requires to be further modification.

Second, the long-term stability and reliability should be considered to ensure the surgical safety, especially in the case of inertial piezoelectric actuators. The creep of the CM would affect the pre-load force applied at the driving point, and then

affect the stability of the NID. Hence, ensuring the stability of the pre-load is an important issue to the productization of this type of NID.

Last, the structure and performance of the driving CM can be further optimized. For one thing, the x-axis positioning platform that provides the pre-load force in the current prototype can be removed, and the optimal pre-load force can be fixed beforehand according to the specific needs. For another thing, the current CM occupies a large plane space, but it still has great potential in spatial structure. Another advantage of the spatial structure of driving CM lies in that it allows the design of multiple driving feet, which may be possible to improve the driving instability phenomenon in high frequency and reduce the inherent backward error of the stick-slip driving mode.

B. Conclusion

To meet the miniaturization and high precision requirements of robotic-assisted needle interventions, a NID based on the inertial piezoelectric actuator is developed and validated in this paper. As far as the authors' knowledge, this is the stick-slip mode NID with the largest insertion force. A wealth of experiments are carried out to validate the insertion performance of the NID and the relationship between insertion parameters and driving parameters is discussed in detail. The result shows that this NID owns a maximum speed of 6.89 mm/s, a maximum insertion force of 2.4 N, and a resolution of 4.7 nm in fine positioning mode.

Further work would focus on the design of the mechanical structure to increase insertion force and control system to ensure insertion accuracy.

REFERENCES

- [1] A. Ebrahimi, S. Sefati, P. Gehlbach, R. H. Taylor, and I. I. Iordachita, "Simultaneous online registration-independent stiffness identification and tip localization of surgical instruments in robot-assisted eye surgery," *IEEE Transactions on Robotics*, vol. 39, no. 2, pp. 1373–1387, 2023.
- [2] "Integral terminal sliding-mode-based adaptive integral backstepping control for precision motion of a piezoelectric ultrasonic motor," *Mechanical Systems and Signal Processing*, vol. 144, p. 106856, 2020.
- [3] Y. Duan, J. Ling, Z. Feng, D. Yao, and Y. Zhu, "Development of a Base-Actuated Three-Rhombus Configured Remote Center of Motion Mechanism for Lumbar Puncture," *Journal of Mechanisms and Robotics*, vol. 16, no. 5, p. 054503, 2023.
- [4] S. Yang, R. A. MacLachlan, and C. N. Riviere, "Manipulator design and operation for a six-degree-of-freedom handheld tremor-canceling microsurgical instrument," *IEEE/ASME Transactions on Mechatronics*, vol. 20, no. 2, pp. 761–772, 2015.
- [5] M. Lu, Y. Zhang, C. M. Lim, and H. Ren, "Flexible needle steering with tethered and untethered actuation: Current states, targeting errors, challenges and opportunities," *Annals of Biomedical Engineering*, vol. 51, no. 5, pp. 905–924, 2023.
- [6] B. Konh, P. Berkelman, and S. Karimi, "Needle tip manipulation and control of a 3d steerable sma-activated flexible needle," in *2020 8th IEEE RAS/EMBS International Conference for Biomedical Robotics and Biomechanics (BioRob)*, Conference Proceedings, pp. 903–909.
- [7] K.-C. Yoon, K. G. Kim, D. C. Lee, and S. J. Yoon, "Smart syringe using actuator and force sensor for epidural anesthesia injection," *International Journal of Artificial Organs*, vol. 45, no. 3, pp. 331–336, 2022.
- [8] Y. Moon, J. B. Seo, and J. Choi, "Development of new end-effector for proof-of-concept of fully robotic multichannel biopsy," *IEEE/ASME Transactions on Mechatronics*, vol. 20, no. 6, pp. 2996–3008, 2015.
- [9] S. Nisar, A. Hameed, N. Kamal, O. Hasan, and F. Matsuno, "Design and realization of a robotic manipulator for minimally invasive surgery with replaceable surgical tools," *IEEE/ASME Transactions on Mechatronics*, vol. 25, no. 6, pp. 2754–2764, 2020.
- [10] M. U. Farooq, B. Xu, and S. Y. Ko, "A concentric tube-based 4-dof puncturing needle with a novel miniaturized actuation system for vitrectomy," *Biomedical engineering online*, vol. 18, no. 1, pp. 1–16, 2019.
- [11] Y. Duan, Y. Zhang, Y. Shen, J. Ling, and Y. Zhu, "A three-rhombus configured remote center of motion mechanism for robot-assisted surgery," in *2022 37th Youth Academic Annual Conference of Chinese Association of Automation (YAC)*, 2022, pp. 930–934.
- [12] H. Su, W. Shang, G. Li, N. Patel, and G. S. Fischer, "An mri-guided telesurgery system using a fabry-perot interferometry force sensor and a pneumatic haptic device," *Annals of Biomedical Engineering*, vol. 45, pp. 1917–1928, 2017.
- [13] B. Qi, Z. Yu, Z. K. Varnamkhasti, Y. Zhou, and J. Sheng, "Toward a telescopic steerable robotic needle for minimally invasive tissue biopsy," *IEEE Robotics and Automation Letters*, vol. 6, no. 2, pp. 1989–1996, 2021.
- [14] E. Perra, E. Lampsjarvi, G. Barreto, M. Arif, T. Puranen, E. Hagstrom, K. P. H. Pritzker, and H. J. Nieminen, "Ultrasonic actuation of a fine-needle improves biopsy yield," *Scientific Reports*, vol. 11, no. 1, pp. 8234–8234, 2021.
- [15] K. El Bannan, B. A. Chronik, and S. P. Salisbury, "Development of an mri-compatible, compact, rotary-linear piezoworm actuator," *Journal of Medical Devices*, vol. 9, no. 1, 2015.
- [16] J. D. Opfermann, M. Barbic, M. Khrenov, S. Guo, N. R. Sarfaraz, J. U. Kang, and A. Krieger, "A novel wax based piezo actuator for autonomous deep anterior lamellar keratoplasty (piezo-dalk)," in *2021 IEEE/RSJ International Conference on Intelligent Robots and Systems (IROS)*, 2021, pp. 757–764.
- [17] J. Ling, L. Chen, Z. Feng, and Y. Zhu, "Development and test of a high speed pusher-type inchworm piezoelectric actuator with asymmetric driving and clamping configuration," *Mechanism and Machine Theory*, vol. 176, p. 104997, 2022.
- [18] B. Zhang, F. Chen, H. Li, Z. Du, and W. Dong, "Development and analysis of a tip-separated flexure needle based on piezo actuation," in *2017 IEEE International Conference on Manipulation, Manufacturing and Measurement on the Nanoscale (3M-NANO)*, Conference Proceedings, pp. 108–112.
- [19] J. Deng, S. Liu, Y. Liu, L. Wang, X. Gao, and K. Li, "A 2-dof needle insertion device using inertial piezoelectric actuator," *IEEE Transactions on Industrial Electronics*, vol. 69, no. 4, pp. 3918–3927, 2022.
- [20] Y. Zhang, Y. Peng, Z. Sun, and H. Yu, "A novel stick-slip piezoelectric actuator based on a triangular compliant driving mechanism," *IEEE Transactions on Industrial Electronics*, vol. 66, no. 7, pp. 5374–5382, 2019.
- [21] C. Qiu, J. Ling, Y. Zhang, M. Ming, Z. Feng, and X. Xiao, "A novel cooperative compensation method to compensate for return stroke of stick-slip piezoelectric actuators," *Mechanism and Machine Theory*, vol. 159, p. 104254, 2021.
- [22] C. Simone, "Modeling of needle insertion forces for percutaneous therapies," Ph.D. dissertation, Citeseer, 2002.
- [23] A. Ebrahimi, F. Alambeigi, S. Sefati, N. Patel, C. He, P. Gehlbach, and I. Iordachita, "Stochastic force-based insertion depth and tip position estimations of flexible fbg-equipped instruments in robotic retinal surgery," *IEEE/ASME Transactions on Mechatronics*, vol. 26, no. 3, pp. 1512–1523, 2020.
- [24] S. Shim, D. Ji, S. Lee, H. Choi, and J. Hong, "Compact bone surgery robot with a high-resolution and high-rigidity remote center of motion mechanism," *IEEE Transactions on Biomedical Engineering*, vol. 67, no. 9, pp. 2497–2506, 2020.
- [25] N. Fati, G. Fitiwi, A. Aynalem, and A. Muche, "Depth of spinal needle insertion and its associated factors among patients who underwent surgery under spinal anesthesia," *Translational Research in Anatomy*, vol. 25, p. 100143, 2021.